Simulation and experimental validation of shear deformation and strength of textile-reinforced composites

Ehsan Shafiei [a] and Ever J. Barbero [b*]

[(a)] Department of Maritime Engineering, Amirkabir University of Technology, No. 350, Hafez Ave, Valiasr Square, Tehran, Iran.

[(b)] Department of Mechanical and Aerospace Engineering, West Virginia University, Morgantown, WV 26506-6106, USA. [*] Corresponding Author

Submitted: 4/28/2021. DOI: 10.1080/15376494.2021.1933277

Abstract

A micro-meso-scale model is proposed to predict shear deformation and strength of textile-reinforced composites, considering shear non-linearity, strain-rate dependent elastic and visco-plastic behavior, and 3D geometrical nonuniformity of the reinforcement. The matrix and fibers are combined using bridging-model micromechanics into composite tows. Combined with the geometrical characteristics of the reinforcement, a composite with orthotropic rate-dependent visco-plastic behavior is obtained. A damage model detects damage in the composite tows and interstitial matrix, introducing stiffness reduction and stress redistribution. The model constants are measured by experiments on neat epoxy matrix and unidirectional glass/epoxy specimens. Model predictions are validated with independent experiments.

Keywords

Micro-scale, Meso-scale, Textile-reinforcement, Shear experiments, Shear fixture

1. Introduction

Textile-reinforced composites are high-performance structural materials that have advantages such as damage tolerance and enjoy growing use in marine, automotive, and aerospace applications. The textile-reinforced composites show significant non-linear stress-strain response under shear loading due to the visco-plastic behavior of the matrix and a complex 3D textile structure. Furthermore, the initial modulus and final strength are loading-rate sensitive. The response of the textile-reinforced composites is accurately predicted herein by

including shear non-linearity, rate-dependency, textile-reinforced internal geometry, and damage effects.

The visco-plastic behavior of the matrix material is found to be the main reason for the shear non-linearity. Various plastic and visco-plastic models have been proposed in the literature to study the shear non-linearity of textile-reinforced composites. Elasto-plastic models using in-plane stress to calculate plastic deformations of the textile-reinforced composite are proposed in [1--3]. Classical Hill plastic criterion and a homogenizing unit cell are used in [4] to calculate yield of the impregnated tows, to further calculate the non-linear behavior of the textile-reinforced composite. Other investigators [5, 6] have stated that the plastic behavior of textile-reinforced composites is dominated exclusively by the in-plane shear stress, thus a potential function was proposed to calculate the non-linear response of textile-reinforced composites. These macro-scale plastic models calculate the equivalent shear non-linearity of a textile-reinforced composite without revealing the quantitative effect of the matrix (interstitial between tows and impregnated between fibers) on the resulting non-linear behavior of the textile-reinforced composite. A micromechanical model including matrix plasticity effects on the mechanical response of the UD composite was proposed in [7]. Potential functions are defined in terms of the hydrostatic stress and 2nd invariant of deviatoric stress to calculate the visco-plastic response of the matrix as per [8--10]. A visco-plastic formulation derived from a potential function in terms of the 1st invariant of stress and the 2nd and 3rd invariants of deviatoric stress was developed in [11] to consider the effects of hydrostatic stress, distortional stresses, and loading angle on the matrix visco-plastic response.

Experimental studies to elucidate the effect of loading rate on the behavior of textile-reinforced composites have been reported in [12, 13] among others. It was shown [12--14] that textile-reinforced laminates have more pronounced non-linear behavior, lower modulus, and lower strength as a function of load angle from 0° to 45°. Furthermore, increasing the strain rate from 10^{-4} to 10^{-2} s^{-1} at 15°, 30° and 45° off-axis load angles causes an increase of strength by about 22%, 13% and 17%, respectively [14]. Peak non-linearity and plastic deformation of textile-reinforced laminates occur at 45° load angle [2, 3, 15, 16]. Using the Iosipescu and two-rail fixtures, it was shown [17, 18] that non-linearity starts at about 1% shear strain, followed by increment of plastic strain, reduction of tangent shear modulus, eventually converging to a horizontal asymptote.

Representative unit cells (RUC) have been proposed to calculate the elastic properties of textile-reinforced composites [7, 19--23]. A three-dimensional RUC includes the interlaced warp and fill composite tows as well as interstitial matrix regions. Early models [24] ignored tow undulation and used approximated rectangular tow cross-sections. A purely micro-mechanics approach was proposed in [25]. Finite element analysis has been used in many studies, including [26] and many more. An RUC using orthotropic tows of elliptical cross-section with undulation was introduced in [23]. More elaborated geometry of the textile-reinforcement, taking into account the gap between adjacent tows in addition to the undulation and elliptical cross section of tows was introduced in [7, 19, 22]. Traction-only visco-plastic behavior of textile-reinforced laminates using a micro-meso-scale model that considers elliptical cross-section, undulation, and gap between adjacent tows, as well as the effects of visco-plastic matrix and visco-elastic fiber was proposed in [27]. Textile reinforcements, also called fabric reinforcements, are also integral part of many studies on sandwich plates, e.g. [28].

The present study proposes a new formulation to simulate shear load effects that produce non-linear and rate-dependent response. The proposed formulation includes a visco-plastic matrix, visco-elastic fibers, damage, and 3D nonuniform geometry of the textile reinforcement as the main reasons for the non-linear rate-dependent response of the textile-reinforced composite. The proposed micro- and meso-scale models include both rate-dependent shear non-linearity and geometrical description of the textile reinforcement. The visco-plastic behavior of the composite tows is predicted by using the proposed micro-scale model including loading-rate effects on the fiber and matrix, and non-linear behavior of the matrix due to shear. Furthermore, the geometric features, cross-section shape, undulation, and stacking sequence of the tows in the meso-scale model result in a composite with orthotropic non-linear rate-dependent visco-plastic behavior. At each differential step, the visco-elasticity of the fiber and visco-plasticity of matrix are updated, and subsequently, the visco-plasticity of the composite tows and the textile-reinforced composite are updated as well.

A simple damage model is incorporated to enhance the prediction of stress-strain response of textile-reinforced composites as a function of strain rates. At the onset of damage in the sub-elements of the RUC, the stiffness matrices of the sub-elements are reduced. Then, the RUC stiffness matrices are updated, and the loads redistributed over the undamaged regions.

The visco-plastic model constants are derived using data from experiments on epoxy matrix and UD glass/epoxy composite at different strain rates. The proposed model is verified using additional independent test data from shear experiments of plain-woven textile-reinforced glass/epoxy composite at various strain rates. Good agreement is found at over the whole range of strain rates covered by the experimental data. The shear experiments on the epoxy and textile-reinforced composite specimens are carried out using a newly designed fixture that improves the performance of previous standard fixtures.

2. Multi-scale model

The proposed multi-scale model consists of a micro-scale model and a meso-scale model. At the micro-scale the composite tows with visco-plastic behavior are modelled as a combination of rate-dependent non-linear visco-plastic matrix and rate-dependent visco-elastic fiber. At the meso-scale, the textile-reinforced composite is modelled as a combination of rate-dependent non-linear visco-plastic tows with undulation, gaps, and interstitial matrix, resulting in a textile-reinforced composite with orthotropic rate-dependent non-linear visco-plastic behavior.

2.1. Micro-scale model

Simulation of visco-plastic composite tows is based on the non-linear rate-dependent mechanical behavior of constituents and their volume fractions. The strain applied on the composite tow is divided into elastic and inelastic parts. Fibers are assumed to have elastic rate-dependent behavior and the matrix has non-linear rate-dependent visco-plastic behavior. The total strain $\{\varepsilon_i\}$ can be divided into elastic $\{\varepsilon_i\}^E$ and inelastic strains $\{\varepsilon_i\}^I$

$$\{\varepsilon_i\} = \{\varepsilon_i\}^E + \{\varepsilon_i\}^I \tag{1}$$

The elastic and inelastic strains are related to the elastic strains of fiber $\{\varepsilon_i^f\}^E$ and matrix $\{\varepsilon_i^m\}^E$, and the inelastic strain of matrix $\{\dot{\varepsilon}_i^m\}^I$ along with volume fraction of fiber v_f and matrix v_m in the composite tow as follows

$$\{\varepsilon_i\}^E = v_f\{\varepsilon_i^f\}^E + v_m\{\varepsilon_i^m\}^E, \quad \{\varepsilon_i\}^I = v_m\{\varepsilon_i^m\}^I \tag{2}$$

The time derivatives of elastic $\{\dot{\varepsilon}_i\}^E$ and inelastic $\{\dot{\varepsilon}_i\}^I$ strain components are

$$\{\dot{\varepsilon}_i\}^E = v_f\{\dot{\varepsilon}_i^f\}^E + v_m\{\dot{\varepsilon}_i^m\}^E, \quad \{\dot{\varepsilon}_i\}^I = v_m\{\dot{\varepsilon}_i^m\}^I \tag{3}$$

For any applied strain rate, the share of strain rate in the fiber $\{\dot{\varepsilon}_i^f\}$ and matrix $\{\dot{\varepsilon}_i^m\}$ as a function of total strain rate in the composite tow $\{\dot{\varepsilon}_j\}$ are calculated using bridging-model micro-mechanics, as follows

$$\{\dot{\varepsilon}_i^f\} = [S_{ij}^f](v_f[S_{ij}^f] + v_m[S_{ij}^m][P_{ij}])^{-1}\{\dot{\varepsilon}_j\} \tag{4}$$

$$\{\dot{\varepsilon}_i^m\} = [S_{ij}^m][P_{ij}](v_f[S_{ij}^f] + v_m[S_{ij}^m][P_{ij}])^{-1}\{\dot{\varepsilon}_j\} \tag{5}$$

where $[S_{ij}^f]$ and $[S_{ij}^m]$ are compliance matrices of fiber and matrix, $[P_{ij}]$ is the bridging matrix [7]. The strain-rate-dependent compliance matrix of the composite tow is described as follows

$$[S_{ij}(\dot{\varepsilon})] = (v_f[S_{ij}^f(\dot{\varepsilon})] + v_m[S_{ij}^m(\dot{\varepsilon})][A_{ij}(\dot{\varepsilon})])(v_f[I_{ij}] + v_m[A_{ij}(\dot{\varepsilon})])^{-1} \tag{6}$$

The bridging matrix defines the load sharing of the fiber and matrix as follows [7]

$$\{\sigma_i^m\} = [P_{ij}]\{\sigma_i^f\}, \quad i, j = 1,...,6 \tag{7}$$

The general form of the bridging matrix with nonzero elements is defined as follows [7]

$$[P_{ij}] = \begin{bmatrix} a_{11} & a_{12} & a_{13} & 0 & 0 & 0 \\ 0 & a_{22} & 0 & 0 & 0 & 0 \\ 0 & 0 & a_{33} & 0 & 0 & 0 \\ 0 & 0 & 0 & a_{44} & 0 & 0 \\ 0 & 0 & 0 & 0 & a_{55} & 0 \\ 0 & 0 & 0 & 0 & 0 & a_{66} \end{bmatrix} \tag{8}$$

$$a_{11} = \frac{E_m^T}{E_{fa}}$$

$$a_{22} = a_{33} = a_{44} = 0.6 + \frac{0.4E_m^T}{E_{ft}} \tag{9}$$

$$a_{55} = a_{66} = 0.5 + \frac{0.5G_m^T}{G_{fa}}$$

$$a_{12} = a_{13} = \frac{(S_{12}^f - S_{12}^m)(a_{11} - a_{22})}{(S_{11}^f - S_{11}^m)}$$

In Eqs. (8) and (9), G_m^T and E_m^T are the shear and Young's tangent modulus of the matrix material that are tangent to the stress-strain curve at each time step. E_{fa}, E_{ft} and G_{fa} are the axial, transverse, and axial shear moduli of the fiber, respectively.

The total strain-rate of the matrix is obtained on the LHS of Eq. (5), but only the inelastic part is affected by visco-plasticity. The inelastic strain rate of the matrix $\dot{\varepsilon}_{ij}^{m^I}$ is calculated by the following visco-plastic constitutive equation [11]

$$\dot{\varepsilon}_{ij}^{m^I} = \frac{2D_0}{3\sigma_e^2} \exp\left[-\frac{1}{2}\left(\frac{Z}{\sigma_e} \right)^{2n} \right] \left[\frac{3}{2}\sigma_{ij}^d \sqrt{J_2} - C(t_{ij}' + 3I_1^2 \delta_{ij}) \right] \tag{10}$$

and the elastic strain rate of the matrix is obtained by subtracting (10) from (5). The inelastic strain rate, Eq. (10), is derived by means of an associated flow rule from the following potential function [11]

$$f = J_2^{3/2} - C(J_3 + I_1^3) \tag{11}$$

The potential function, Eq. (11), is expressed in terms of second J_2 and third J_3 invariants of the deviatoric stress tensor, and the first invariant I_1 of the stress tensor, while *Z*, *C*, D_0 and *n* in Eq. (10) are material constants (Table 1). Additionally, σ_e is the effective stress and t_{ij}' is derivative of J_3 respect to the deviatoric stress. Additional details of the procedure for deriving Eq. (10) and characterization of its parameters are described in [11].

The constitutive equation to describe the stress-strain relation in sub-elements at each differential step according to Eqs. (3), (6), and (10), is defined as

$$\{\sigma\} = [C_{ij}] \left\{ \varepsilon - \upsilon_m \varepsilon^{m^I} \right\} \tag{12}$$

where $[C_{ij}]$ is $[S_{ij}]^{-1}$ obtained from Eq. (6), ε is the applied strain on sub-elements, υ_m and ε^{m^I} are Poison's ratio and inelastic strain of matrix from Eq. (10).

2.2. Meso-scale unit cell

The meso-scale model comprises a representative unit cell (RUC) used to calculate the stiffness matrices of the textile-reinforced lamina. The rate-dependent visco-plastic properties

of the textile-reinforced composite are calculated at the meso-scale where the composite tows are modeled as off-axis UD composites. Meso-scale simulation is based on an RUC that defines the geometry of the composite tows, orientation, and their stacking sequence. The RUC simulates rate-dependent visco-plastic response of the textile-reinforced lamina. The RUC is the smallest element that is extracted from a repetitive unit cell (RUC) of the textile-reinforced lamina, Fig. 1. The RUC of the plain-weave reinforced lamina has two symmetrical planes that reduce the required size for analysis to a quarter RUC, Fig. 2(a). Furthermore, the quarter RUC has anti-symmetric planes that allows us to reduce the RUC to 1/16 of the RUC [29] as shown in Fig. 2(b).

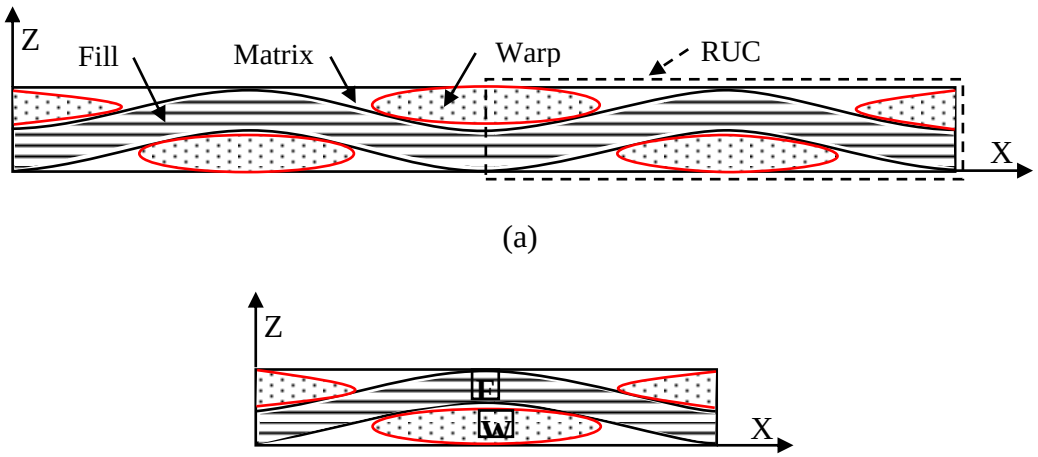

Fig. 1. (a) Cross-section of (a) textile-reinforced layer, (b) selected RUC.

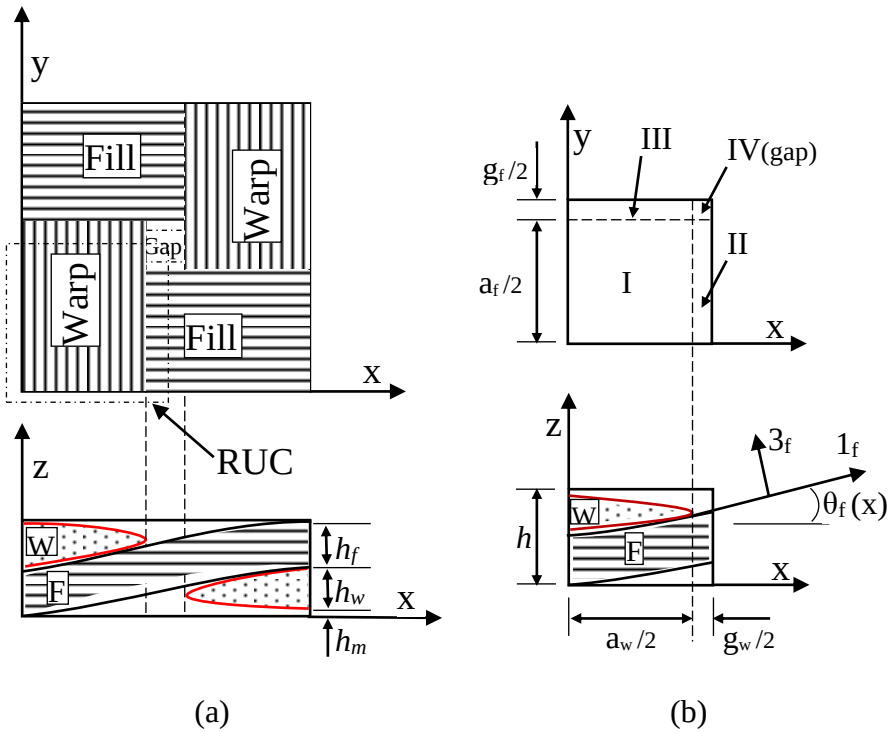

(a) (b)

Fig. 2. Top and side views of (a) one quarter RUC, (b) RUC with details.

The boundary surfaces of the warp and fill tows are defined as [19, 29]

$$z_w^{upper/lower}(x,y) = -\frac{h_w}{2}\cos\frac{\pi y}{a_f+g_f} \pm \frac{1}{2}\left|h_w\cos\frac{\pi x}{a_w}\right| \quad \text{for } x\in[0,\frac{a_w}{2}] \tag{13}$$

$$z_f^{upper/lower}(x,y) = -\frac{h_f}{2}\cos\frac{\pi x}{a_w+g_w} \pm \frac{1}{2}\left|h_f\cos\frac{\pi y}{a_f}\right| \quad \text{for } y\in[0,\frac{a_f}{2}] \tag{14}$$

The superscript *upper* and *lower* denote upper and lower boundary surfaces of the composite tows. Subscripts w, f, and m in Fig. 2 and Eqs. (13) and (14) represent the warp and fill tows, and matrix sub-element. The local undulated angle of warp θ_w and fill θ_f tows are calculated as derivative of Eqs. (13) and (14)

$$\theta_w(y) = \left|\arctan\left(\frac{d}{dy}z_w(y)\right)\right| \tag{15}$$

$$\theta_f(x) = \left|\arctan\left(\frac{d}{dx}z_f(x)\right)\right| \tag{16}$$

The occupied volumes of the warp V_w and fill tows V_f are calculated by the double integration of the cross-sectional area multiplied by the undulated length of tows

$$V_w = \int_0^{\frac{a_f+g_f}{2}} \int_0^{\frac{a_w+g_w}{2}} h_w \sqrt{1+\left(\frac{d}{dy} z_w(y)\right)^2} \cos\frac{\pi x}{a_w} dxdy \tag{17}$$

$$V_f = \int_0^{\frac{a_w+g_w}{2}} \int_0^{\frac{a_f+g_f}{2}} h_f \sqrt{1+\left(\frac{d}{dx} z_f(x)\right)^2} \cos\frac{\pi y}{a_f} dydx \tag{18}$$

Assuming the fill and warp tows have the same fiber volume fraction v_f, the fiber volume fraction is calculated as a function of the overall fiber volume of the textile-reinforced composite v_f^c as follows

$$v_f = v_f^c \frac{h(a_w+g_w)(a_f+g_f)}{4(V_w+V_f)}, \quad v_m = 1-v_f, \quad h = h_w + h_f + h_m \tag{19}$$

2.2. Meso-scale stiffness

The rate-dependent visco-plastic properties of the composite tows, Eq. (6), and the geometrical characteristics of composite tows defined in section 2.1 are used to calculate the rate-dependent visco-plastic properties of the textile-reinforced composite. To reduce the computational effort, the RUC is divided into four regions, I to IV, with different stacking sequence [19, 29], Fig. 2(b). From bottom to top, the stacking sequence for regions are I: matrix/fill/warp/matrix, II: matrix/fill/matrix, III: matrix/warp/matrix, and IV: pure matrix. Each region is treated as a laminated composite with strain-rate-dependent stiffness matrices $[A_{ij}(\dot{\varepsilon}, x, y)], [B_{ij}(\dot{\varepsilon}, x, y)]$, and $[D_{ij}(\dot{\varepsilon}, x, y)]$. The values of the stiffness matrices vary over the (x,y) coordinates of the RUC surface due to the undulation of composite tows, which is taken into account by the through-the-thickness integration of transformed stiffness matrices $[C'_{ij}(\dot{\varepsilon}, x, y)]$ of the warp, fill and matrix layers, as follows

$$[A_{ij}(\dot{\varepsilon}, x, y)], [B_{ij}(\dot{\varepsilon}, x, y)], [D_{ij}(\dot{\varepsilon}, x, y)] = \int_{-h/2}^{h/2} (1, z, z^2)[C'_{ij}(\dot{\varepsilon}, x, y)]dz \quad i, j = 1, ..., 6 \tag{20}$$

where $[C'_{ij}] = [S'_{ij}]^{-1}$. The transformed compliance matrix $[S'_{ij}]^{-1}$ is obtained from Eq. (21) and compliance matrix $[S_{ij}]$ for the matrix and composite tow are obtained from Eq. (6), as follows

$$[S'_{ij}(\dot{\varepsilon}, x, y)] = [T_{ij}(x, y)]^T [S_{ij}(\dot{\varepsilon}, x, y)][T_{ij}(x, y)] \tag{21}$$

The transformation matrices for the warp and fill tows, $[T_{ij}(x, y)]_w$ and $[T_{ij}(x, y)]_f$, are given in terms of the sine and cosine functions of the warp and fill undulation angles $\theta_w(y)$ and

$\theta_f(x)$. The strain-rate-dependent stiffness matrices of the textile-reinforced composite, $[\bar{A}_{ij}(\dot{\varepsilon})], [\bar{B}_{ij}(\dot{\varepsilon})]$ and $[\bar{D}_{ij}(\dot{\varepsilon})]$, are then obtained by a double integration of local stiffness matrices, Eq. (20), over the four regions of the RUC, as follows

$$[\bar{A}_{ij}(\dot{\varepsilon})], [\bar{B}_{ij}(\dot{\varepsilon})], [\bar{D}_{ij}(\dot{\varepsilon})] = \frac{4}{(a_w+g_w)(a_f+g_f)} \times \int_0^{(a_w+g_w)/2} \int_0^{(a_f+g_f)/2} \left([A_{ij}(\dot{\varepsilon},x,y)], [B_{ij}(\dot{\varepsilon},x,y)], [D_{ij}(\dot{\varepsilon},x,y)]\right) dxdy \tag{22}$$

The strain-rate dependent tensile and shear moduli, and Poison's ratio of the textile-reinforced laminated composite in *x* and *y* directions are calculated using the in-plane stiffness matrix $[\bar{A}_{ij}(\dot{\varepsilon})]$ as follows

$$E_x(\dot{\varepsilon}) = \frac{\bar{A}_{11}(\dot{\varepsilon})\bar{A}_{22}(\dot{\varepsilon}) - \bar{A}_{12}^2(\dot{\varepsilon})}{h\bar{A}_{22}(\dot{\varepsilon})}, E_y(\dot{\varepsilon}) = \frac{\bar{A}_{11}(\dot{\varepsilon})\bar{A}_{22}(\dot{\varepsilon}) - \bar{A}_{12}^2(\dot{\varepsilon})}{h\bar{A}_{11}(\dot{\varepsilon})},$$
$$G_{xy}(\dot{\varepsilon}) = \frac{\bar{A}_{66}(\dot{\varepsilon})}{h}, \ \nu_{xy} = \frac{\bar{A}_{12}(\dot{\varepsilon})}{\bar{A}_{22}(\dot{\varepsilon})} \tag{23}$$

Experimental data of modulus and strength of fibers and UD composite tows is obtained at discrete strain rates in Section 4. Values of modulus and strength at other strain rates are calculated as

$$A(\dot{\varepsilon}) = A_0[1 + B\ln(\frac{\dot{\varepsilon}}{\dot{\varepsilon}_0})] \tag{24}$$

where A is the target mechanical property, modulus or strength, A_0 is the value of A at the reference strain rate $\dot{\varepsilon}_0$, and B is a material constant that is calculated by fitting the experimental data.

3. Damage

At the onset of material failure, the stiffness matrix is degraded using a degradation factor and the applied load is redistributed over the intact elements. Failure detection is based on the local stress values in the composite tows and matrix. To reach accurate strength predictions, the four regions of the RUC are meshed into $N \times M$ elements along *x* and *y* directions, Fig. 3. Using the iso-strain assumption [19, 29, 30], the in-plane strains $\{\varepsilon_x, \varepsilon_y, \varepsilon_{xy}\}^T$ applied on the textile-reinforced composite are uniformly and constantly applied to all the elements.

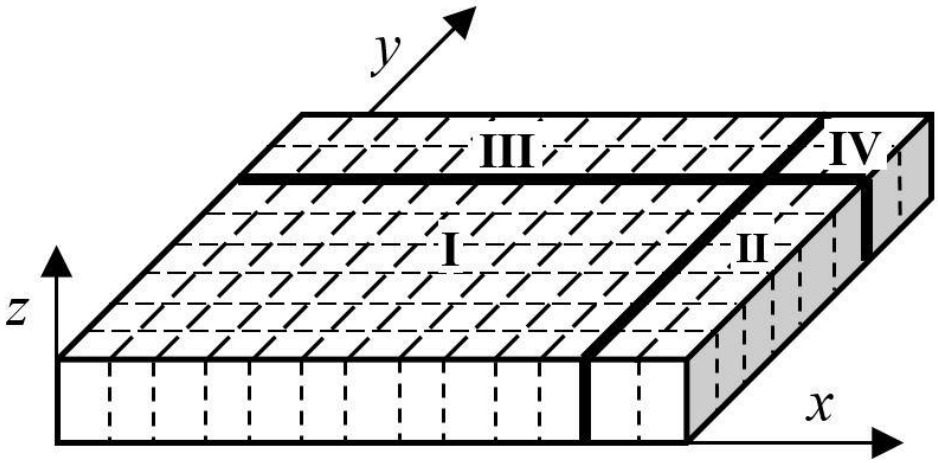

Fig. 3. RUC showing the four regions used for discretization, as in Fig. 2(b).

The load-carrying capacity of the textile-reinforced composite is calculated by predicting the onset of failure of the sub-elements, composite tows, and matrix, at the occurrence of single or simultaneous multiple damage modes. For a combination of shear and transverse loading, the modes of failure of the composite tows and matrix are predicted by using the following criterion, developed by extending the Hashin failure criterion to rate-dependent stress and strength and applying it at each time step of the incremental analysis, in order to account for shear non-linearity and rate-dependence

$$I = \left(\frac{\langle \sigma_{22}(\dot{\varepsilon}^{(n)})\rangle_{+}}{F_{2t}(\dot{\varepsilon}^{(n)})}\right)^2 + \left(\frac{\tau_{12}(\dot{\varepsilon}^{(n)})}{F_6(\dot{\varepsilon}^{(n)})}\right)^2 + \left(\frac{\tau_{23}(\dot{\varepsilon}^{(n)})}{F_4(\dot{\varepsilon}^{(n)})}\right)^2 \geq 1 \tag{25}$$

where $\sigma_{22}(\dot{\varepsilon}^{(n)}), \tau_{12}(\dot{\varepsilon}^{(n)})$ and $\tau_{23}(\dot{\varepsilon}^{(n)})$ are the strain-rate dependent stress components of sub-elements in the local coordinate system at the time step (n). Furthermore, $F_{2t}(\dot{\varepsilon}^{(n)})$, $F_6(\dot{\varepsilon}^{(n)})$ and $F_4(\dot{\varepsilon}^{(n)})$ are rate-dependent transverse tensile, in-plane and out-of-plane shear strengths of sub-elements, respectively. In addition, the subscript t refers to the tension, and the Macaulay operator $\langle\,\rangle$ cancels the first term when the transverse stress is compressive.

3.1. Transverse damage degradation

The experimental data presented in section 5, shows that the early signs of failure in the transverse composite tows occurs in the transverse direction and that matrix cracking causes that failure. Transverse damage occurs without fiber breakage [31]. Friction between fiber and matrix prevents composite tows from losing all their load-carrying capacity. In [17], it is

suggested that under *in-plane shear*, the transverse and shear moduli should be reduced to $d_m=0.01$ of their initial values but in this work we found that a degradation factor $d_m=0.93$ yields better predictions. The onset of transverse failure is the sign of the first matrix cracking, which means that the composite is still capable of carrying further load and the stiffness should not be reduced dramatically but slowly [32, 33].

When the failure criterion, Eq. (25), is satisfied in a composite tow or interstitial matrix, their shear modulus is degraded like this: $G_{dt+1} = d_m G_{dt}$, where d_m is the degradation factor. A value of $d_m=0.93$ is found to provide the best comparison to experimental data (Section 5.4). After failure in the sub-elements, the corresponding stiffness matrix of the elements and consequently the RUC stiffness matrix are updated. Then, the applied load is redistributed over the undamaged elements. The proposed damage propagation method is verified by experimental data in the Section 5.4.

4. Materials and Methods

To predict the behavior of the textile-reinforced composite at various strain rates, the proposed model requires rate-dependent visco-plastic properties of fiber and matrix. In this study, they are extracted from strain-rate-dependent experiments on epoxy matrix and glass/epoxy UD composite.

Additional strain-rate-dependent experiments are carried out on plain-woven-reinforced glass/epoxy textile-reinforced laminates to validate the proposed model. Epolam 2017 resin and Epolam 2018 hardener are used in this study. The physical properties and fabrication methods of the specimens are described in [11]. The parameters describing the geometry of the woven glass textile are shown in Table 2 and Figure 2.

Table 2. Geometrical properties of woven glass textile

Warp tow			Fill tow		
a_w (mm)	h_w (mm)	g_w (mm)	a_f (mm)	h_f (mm)	g_f (mm)
3.5	0.45	0.025	3.5	0.45	0.025

Laminates were fabricated using six layers of plain-weave textile reinforcement. There is no shift between adjacent layers ([29], Fig. 9.10). Uniform impregnation of the textile reinforcement, as well as minimization of cavities and poor or resin-rich regions were achieved by using vacuum infusion. Furthermore, resin and hardener were degassed prior to injection. Table 2 shows the properties of the textile-reinforced laminates. The matrix burn-off method (ASTM D3171) is used to calculate the *overall* fiber volume fraction values reported in Table 3.

Table 3. Properties of manufactured textile-reinforced laminate

Material	Code	Number of Layers	Laminate Thickness (mm)	Overall fiber volume fraction
textile-reinforced Laminate	G-5	6	2.6	0.55
	G-7	6	2.5	0.56

The mechanical behavior of the textile-reinforced composite and epoxy matrix are studied under rate-dependent loadings. Dimensions of specimens are listed in Table 4.

Table 4. Specimen dimensions

	Material	
	textile-reinforced composite	Epoxy
Tensile specimens	-	35×250 (mm)
Shear specimens	75×70 (mm)	75×70 (mm)

Table 5 shows the five displacement rates used in the experiments with textile-reinforced and neat resin specimens. The resulting strain rates are based on the displacement rates and sizes of various specimens. ASTM D3039 and ASTM D7078 standards are followed for tensile and shear experiments in an Instron 8802 UTS.

Table 5. Displacement rates

Material	Displacement rates
textile-reinforced composite	2, 20, 200, 2000, 3240 (mm / min)
Epoxy	3, 30, 300, 2000, 3000 (mm / min)

4.1 Shear fixture

A new fixture, shown in Fig. 4, was designed and fabricated to perform shear experiments on neat matrix and textile-reinforced composite specimens. We experienced difficulties with the fixture proposed in ASTM D7078 because a small misalignment of the specimen may introduce a spurious bending moment that yields noticeable errors and scatter of the test results. The new fixture is designed to achieve automatic alignment of the specimen, ease of clamping the test specimen in the fixture, and ease of mounting the fixture in the hydraulic grips of the Instron 8802 testing machine. The test specimen is automatically aligned inside the two components of fixture, which allows shear to be applied to the specimen while minimizing any bending moment that may accrue due to misalignment of the specimen.

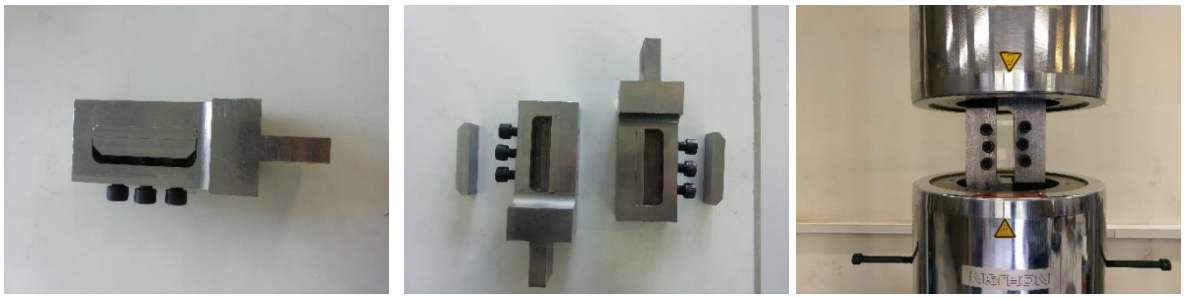

(a) (b) (c)

Fig. 4. (a) and (b) newly designed fixtures for shear deformation experiments, (c) fixtures in tension machine.

5. Results and Discussion

Strain-rate dependent experiments are used to collect data to characterize the matrix material and the glass fibers using neat matrix specimens and UD composite specimens, respectively. The data is used in the proposed model. Separately, shear experiments on textile-reinforced composite specimens at various strain rate are carried out to verify the proposed model. All the experimental material properties needed to reproduce the results are available in this

paper. Matrix: Tables 5, 6, 9. Fibers: Eqs. (26-27). UD composite: UD: Eqs. (28-30). Textile geometry: Table 1. Laminate data used for validation: Figure 5 and Table 8.

5.1. Matrix shear

The characterization and simulation of visco-plastic behavior of the epoxy matrix, based on Eq. (10), requires tensile and shear experiments at different strain rates. The dimensions of the tensile and shear specimens are 130×35 mm and 25×70 mm, respectively, with a thickness of 5 mm.

The experimental tensile and shear stress-strain curves at five strain rates are shown in Fig. 6 (a) and (b). The tensile stress-strain curves with slight curvature are repeated for different tensile strain rates and ended with sudden fracture. The data shows less curvature at higher strain rate respect to the low strain rate. At lower strain rate, the stress-strain curve approaches a straight line. Unlike tensile experiments, shear stress-strain curves with significant non-linearity are observed even at low strain rates. The stress-strain curves converge to a horizontal line, at the yield stress, meaning that the saturation stress and strength converge. The values of the initial modulus, strength, and failure strain for tensile and shear loading at various strain rates are reported in Tables 6 and 7.

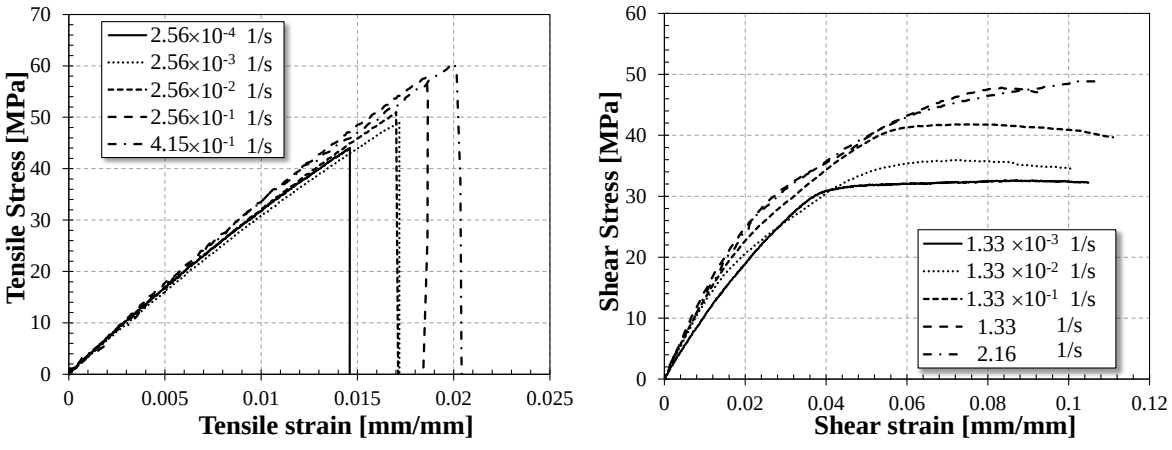

(a) (b)

Fig. 6. (a) Tensile experiments, (b) shear experiments of epoxy matrix at various strain rates [11]

Table 6. Tensile data of initial modulus, strength, and failure strain of epoxy matrix at five strain rates [11]

Strain rate [s^{-1}]	Initial modulus [GPa]	Strength [MPa]	Failure strain
2.56×10^{-4}	3.20	44.1	0.015
2.56×10^{-3}	3.17	49.2	0.017
2.56×10^{-2}	3.28	51.0	0.017
2.56×10^{-1}	3.36	57.9	0.019
4.15×10^{-1}	3.39	60.5	0.021

Table 7. Shear data of initial modulus, strength, and failure strain of epoxy matrix at five strain rates [11]

Strain rate [s^{-1}]	Initial modulus [GPa]	Strength [MPa]	Failure strain
1.33×10^{-3}	1.26	32.2	0.105
1.33×10^{-2}	1.29	35.9	0.100
1.33×10^{-1}	1.32	41.6	0.111
1.33	1.39	47.7	0.092
2.16	1.42	48.9	0.105

The strain-rate dependency of the tensile and shear moduli and strengths are shown in Figs. 6 and 7. Increasing strain rate leads to increase the overall slope of the tensile stress-strain curve, so that the initial modulus and strength increase about 6.9% and 37.5%, respectively, for increasing strain rate from $2.56\times10^{-4}\ s^{-1}$ to $4.15\times10^{-1}\ s^{-1}$, Fig. 7 (a) and (b).

The shear stress-strain data in Fig. 8 (a) and (b) shows more rate dependency over three decades of increasing strain rate from $1.33\times10^{-3}\ s^{-1}$ to $2.16\ s^{-1}$, which the shear modulus and strength increase about 12% and 51.7%. The scattering of the tensile and shear moduli is negligible, but the tensile and shear strengths have maximum scattering about 5% and 6%, as shown by error bars.

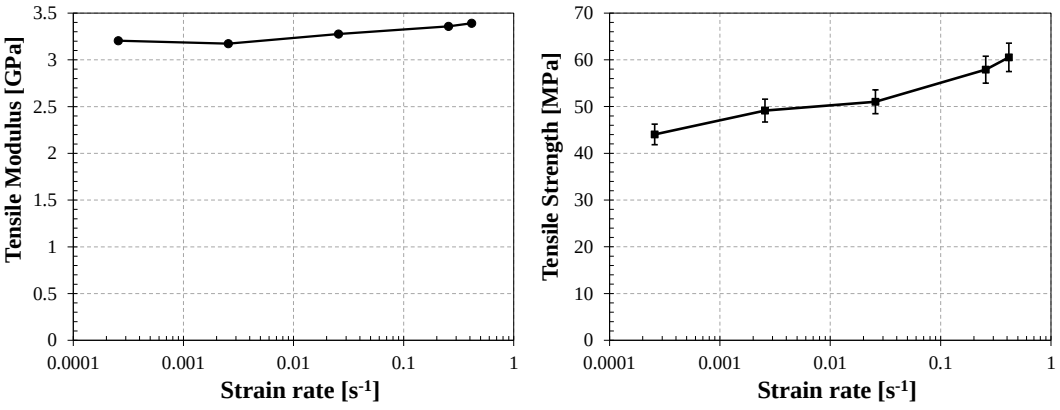

(a) (b)

Fig. 7. Shear strain rate on (a) tensile initial modulus, (b) tensile strength of epoxy matrix [11]. Strain-rate range from 2.56 10^{-4} to 4.15 10^{-1} s^{-1}.

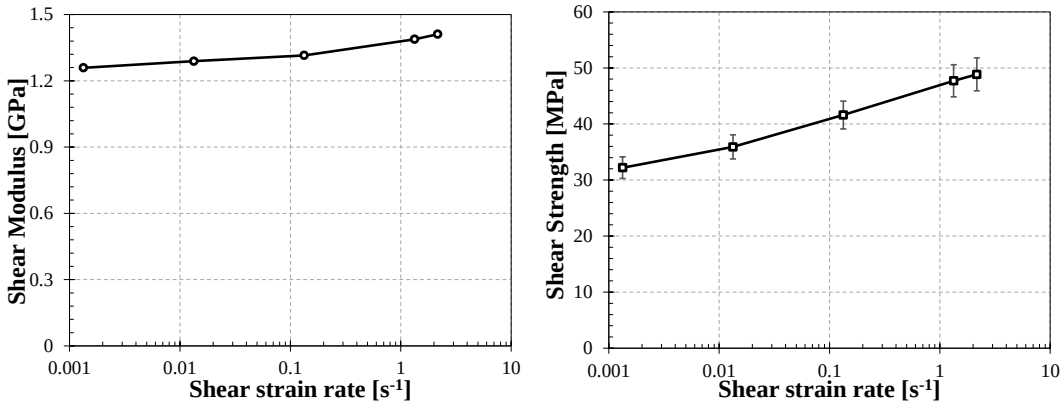

(a) (b)

Fig. 8. Effect of shear strain rate on (a) initial shear modulus, (b) shear strength of epoxy matrix [11]. Strain-rate range from 1.33 10^{-3} to 2.1 s^{-1}.

5.2. Laminate shear

In this study, shear-test specimens of textile-reinforced laminates with dimensions 25×70 mm are tested under pure in-plane shear loading with changing strain rate from 2×10^{-3} to 2 s^{-1} corresponding to displacement rates from 3 to 3000 mm/min. Two textile-reinforced laminates, Table 3, are used to perform experiments with five shear strain rates. Due to the slight difference in fiber volume fraction of between laminates, Table 9 shows which laminate was used for each shear strain rate. The shear test specimens are shown in Fig. 9. To ensure repeatability of the shear stress-strain data, each strain rate is repeated three times. The

rate-dependent shear behaviors of the textile-reinforced laminate are experimentally compared at five strain rates, Fig. 10.

Table 9. Strain rates calculated from displacement rates and specimen dimensions.

textile-reinforced laminate Code	Applied strain rate (s^{-1})
G-5	$2\times10^{-3}, 2\times10^{-2}, 2\times10^{-1}, 1.33$
G-7	2

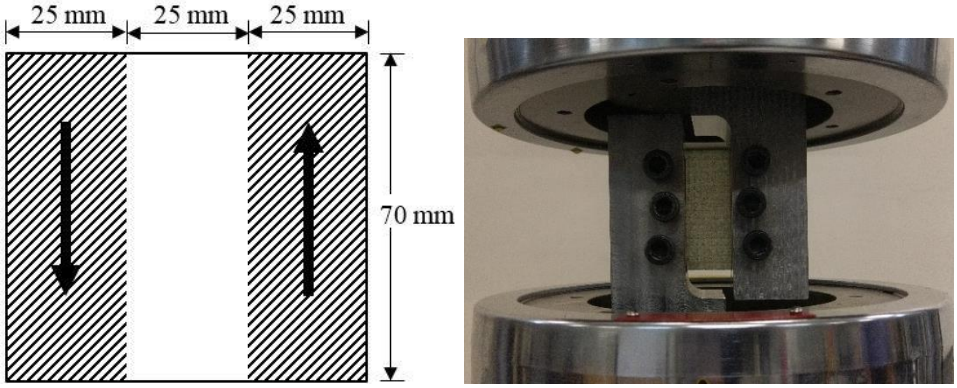

(a) (b)

Fig. 9. Shear test specimen of textile-reinforced laminate. (a) Schematic dimensions, (b) intact specimen mounted on the fixture

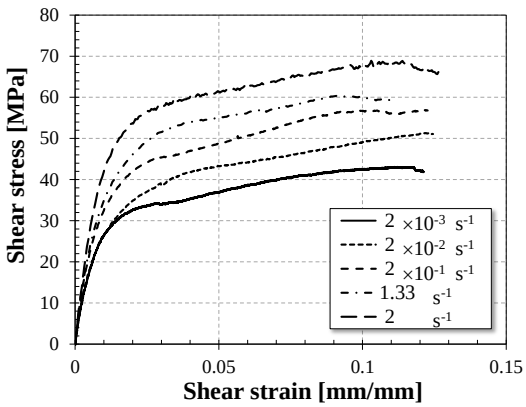

Fig. 10. Shear stress-strain curves of textile-reinforced laminate performed at five strain rates

The non-linear region of the shear stress-strain curve is noticeable even at small strain rate. According to the iso-stress hypothesis, the applied shear stress on the composite tow is transmitted equally to the fiber and matrix. Therefore, for the same shear stress, the glass fibers are almost visco-elastic, and the visco-plastic behavior of the matrix dominates the non-linear rate-dependent shear behavior of composite. Two main features of the shear stress-strain curves, the initial shear modulus and final strength, show rate-sensitivity as shown in Fig. 11 (a) and (b). Under increasing strain rate from 2×10^{-3} to 2.0 s^{-1} the initial shear modulus increases about 38%, and shear strength about 64%. The shear strength data has a scatter of about 7%, shown by the error bars in Fig. 11 (b). The scatter of the shear modulus is less that 3%. The values of the initial modulus, strength, and failure strain for shear loading at different strain rates are reported in Table 8 OK.

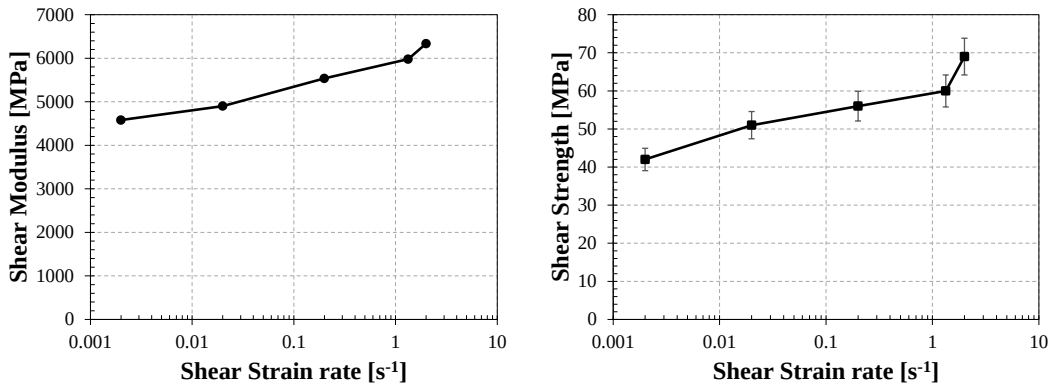

(a) (b)

Fig. 11. Shear rate-dependent behavior (a) Initial modulus, (b) strength. Range from 2 10^{-3} to 2.0 s^{-1}.

Table 8. Experimental values of initial modulus, strength, and failure strain for textile-reinforced composite at various shear strain rates.

Strain rate [s^{-1}]	Initial modulus [GPa]	Strength [MPa]	Failure strain
2×10^{-3}	4.580	42	0.121
2×10^{-2}	4.900	51	0.125
2×10^{-1}	5.537	56	0.123
1.33	5.979	60	0.108
2	6.335	69	0.126

Fractured shear specimens under different shear strain rates are shown in Fig. 11. Each specimen is marked with a letter and its applied strain rate. In all test specimens, the crack starts from the middle of the specimen and propagates along an oblique plane at about 30-45 degrees. The crack continues up to the edges of the specimen, ending at the point of contact with the fixture, then continues to grow parallel to the fixtures until it reaches the ends of the specimen.

In Fig. 12, the surface of specimen (A) with shear strain rate 2×10^{-1} was painted with black color. White spots can be observed in Fig. 12 (A). These white spots are thought to be small cracks in the warp and fill composite tows, as well as regions of matrix plasticity. The micro-scale matrix plasticity and cracking smoothly spreads over the laminate surface and leads to remarkable irreversible deformation in the middle of specimens along the oblique plane. The failure process continues with fiber-matrix debonding. Finally, the fibers break along an oblique plane. This shows that the degradation method described in section 3.1. should only gradually degrade the stiffness of the composite.

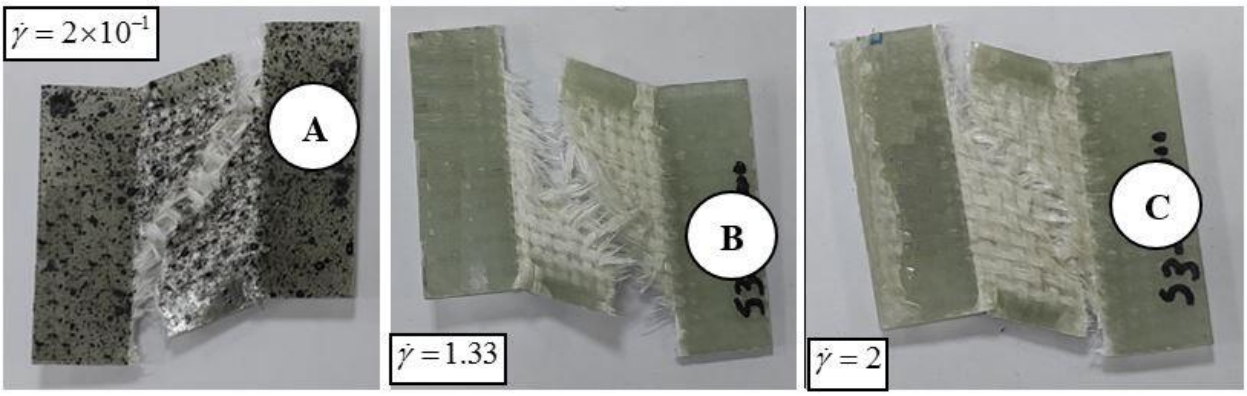

Fig. 12. Failed specimens at different shear strain rates

5.4. Predictions

Rate-dependent visco-plastic properties of the matrix, fiber, and UD composite are required to use the model described in Section 2. The visco-plastic behavior of the matrix is described by the visco-plastic constitutive equation (10), using the material constants in Table 1.

Table 1. Model parameters for the epoxy matrix [11]

D_0 [s^{-1}]	Z_0 [MPa]	Z_1 [MPa]	n	q	C
10^6	627.2	1105.2	0.52	80.1	-1

The longitudinal initial modulus $E_{fa}(\dot{\varepsilon}^f)$ and strength $S_{fa}(\dot{\varepsilon}^f)$ of the glass fiber are described at different strain rates by fitting the experimental data as follows [11]

$$E_{fa}(\dot{\varepsilon}^f) = 55885[0.0019\ln(\frac{\dot{\varepsilon}^f}{2.38\times10^{-4}})+1] \quad [\text{MPa}] \quad \dot{\varepsilon}^f \geq 2.38\times10^{-4}\ (\text{s}^{-1}) \tag{26}$$

$$S_{fa}(\dot{\varepsilon}^f) = 1186.7[0.0464\ln(\frac{\dot{\varepsilon}^f}{2.38\times10^{-4}})+1] \quad [\text{MPa}] \quad \dot{\varepsilon}^f \geq 2.38\times10^{-4}\ (\text{s}^{-1}) \tag{27}$$

The shear modulus $G_{fa}(\dot{\varepsilon}^f)$ of glass fibers at different strain rate are calculated from $E_{fa}(\dot{\varepsilon}^f) = 2G_{fa}(\dot{\varepsilon}^f)(1+\upsilon_f)$, where υ_f is the Poisson's ratio of glass fibers, υ_f =0.3.

The progressive damage model needs the strength values of the UD glass/epoxy composite at various strain rates. The longitudinal $F_{1t}(\dot{\varepsilon})$, transverse $F_{2t}(\dot{\varepsilon})$, and in-plane shear strengths $F_6(\dot{\varepsilon})$ of the UD glass/epoxy composite are described by fitting the experimental data as follows [27]

$$F_{1t}(\dot{\varepsilon}) = 797.98[0.0465\ln(\frac{\dot{\varepsilon}}{2.38\times10^{-4}})+1] \quad (MPa) \quad \dot{\varepsilon} \geq 2.38\times10^{-4}\ (s^{-1}) \tag{28}$$

$$F_{2t}(\dot{\varepsilon}) = 47.673[0.0344\ln(\frac{\dot{\varepsilon}}{2\times10^{-3}})+1] \quad (MPa) \quad \dot{\varepsilon} \geq 2\times10^{-3}\ (s^{-1}) \tag{29}$$

$$F_6(\dot{\varepsilon}) = 39.42[0.0315\ln(\frac{\dot{\gamma}}{10^{-3}})+1] \quad (MPa) \quad \dot{\gamma} \geq 10^{-3}\ (s^{-1}) \tag{30}$$

The shear behavior of the textile-reinforced composite is predicted with the model proposed in Section 2. Comparisons between experimental and predicted shear stress-strain curves at various strain rates are presented in Fig. 5, where the proposed model predicts the shear stress-strain curves at various strain rates with reasonable accuracy. Notably, the initial modulus and final strength of the textile-reinforced composite at different strain rates are

predicted quite accurately. Comparison between predicted and experimental shear initial moduli and strengths at five strain rates are presented in Table 10.

Table 10 OK. Comparison between predicted experimental data of shear initial modulus and strength.

	Initial modulus [GPa]			Strength [MPa]		
Strain rate (s^{-1})	Experimental	Prediction	Error [%]	Experimental	Prediction	Error [%]
2×10^{-3}	4.58	4.57	3.7	43.4	46.9	8.1
2×10^{-2}	4.90	5.13	4.7	51.0	48.9	4.1
2×10^{-1}	5.54	5.76	3.9	57.0	57.8	4.1
1.33	5.98	6.19	3.5	60.	58.8	2.0
2	6.33	6.43	1.6	69.0	68.2	1.2

The predicted stress-strain curves agree with the experimental data very well as shown. In Fig. 5 (b), region I highlights the agreement of initial modulus, region II highlights the initiation of non-linear behavior, region III illustrates how the laminate is reaching saturation stress, and region IV highlights the agreement of final strength. These four regions are the key factors for predicting the shear stress-strain curve. In Fig. 5(b), the matrix enters the non-linear region at about 0.06 shear strain and reaches saturation at about 0.1 strain.

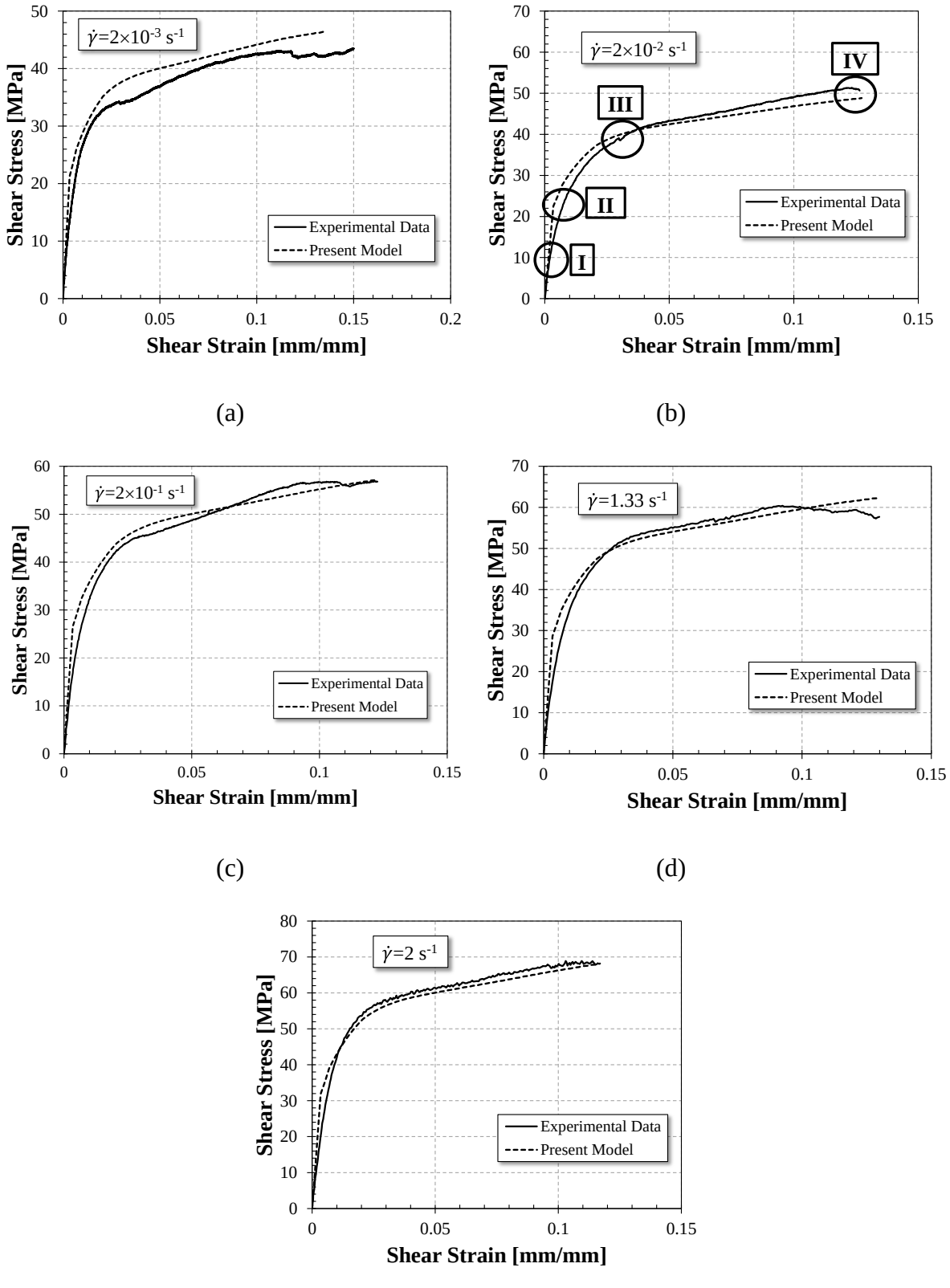

Fig. 5. Comparison between prediction and experimental shear data.

6. Conclusions

A novel micro-meso-scale model with progressive damage is developed to simulate the shear behavior of textile-reinforced composites. The proposed model predicts the rate-dependent visco-plastic behavior of the textile-reinforced composite considering both non-linear material behavior and the complex geometry of the reinforcement. In the micromechanical model, UD composite tows are modeled as a combination of visco-elastic glass fiber and visco-plastic matrix, both rate-dependent. The meso-scale model incorporates visco-plastic composite tows from the micro-model and 3D textile architecture to represent a textile-reinforced composite with orthotropic non-linear rate-dependent visco-plastic behavior. At each differential step, the visco-elastic deformation of the glass fiber and the visco-plastic deformation of the matrix are updated. The progressive damage model detects the onset of failure in the composite tows and interstitial matrix sub-elements. The stiffness matrices of the sub-elements are degraded and the stiffness matrices of the damaged elements and the whole RUC are updated, with stress redistributed over the intact elements. The visco-plastic model constants are obtained from strain-rate-dependent experiments on the matrix and UD composite. Then, shear test data at various stain rates from textile-reinforced laminates is used to verify the proposed model. A newly designed fixture is used to perform shear experiments on the matrix and textile-reinforced composite specimens. Based on the analytical and experimental results, the following observations are noted:

- The predicted values of the initial modulus and strength at various strain rates compare well with experimental data.

- The effects of matrix damage, represented by a degradation factor $d_m=0.93$, is less severe than previously thought ($d_m=0.01$).

- The rate-dependent mechanical response of the textile-reinforced composite stems from different rate-dependency of the fiber and matrix. Their behavior and load-share are included in the micro-scale model. The micro-modelled composite tows with rate-dependent non-linear visco-plastic behavior are then integrated in the meso-scale model.

- The non-linearity of the matrix is found to strongly affect the response of the textile-reinforced laminate over the entire range of applied strain (Fig. 5, a, b, c, d, e).

- The predicted non-linear stress-strain response of the textile-reinforced composites compares well with the experimental data (Fig. 5). The predictions illustrate four regions in

Fig. 5 (b). Region I: initial modulus, region II: onset of non-linearity, region III: reaching saturation stress, and region IV: strength.

• The fracture patterns of the textile-reinforced composite show that there is no sign of major damage in the composite tows prior to final fracture. Damage is smoothly distributed over the specimens, leading to the large deformations. This irreversible deformation leads to an oblique fracture plane that propagates at the center gauge.

Credit authorship contribution statement

Ehsan Shafiei: Conceptualization; Methodology; Resources; Investigation; Data curation; Data validation; Formal analysis; Original draft.

Ever J. Barbero: Advising, Review & Editing.

Acknowledgement: This research did not receive any specific grant from funding agencies in the public, commercial, or not-for-profit sectors.

Data availability:

All the experimental data needed to reproduce the results in this paper is available in the body of this papers, as follows. Matrix properties: Tables 5, 6, 9. Fiber properties: Eqs. (26-27). UD composite properties: UD: Eqs. (28-30). Textile geometry: Table 1. Laminate data used for validation: Figure 14 and Table 8.

References

[1] K. Chung , H. Ryou. "Development of visco-elastic/rate-sensitive-plastic constitutive law for fiber-reinforced composites and its applications. Part I: Theory and material characterization." Composites science and technology 69 (2009) 284-291.
[2] S. Ogihara , K. L. Reifsnider. "Characterization of nonlinear behavior in woven composite laminates." Applied composite materials 9 (2002) 249-263.
[3] S. V. Thiruppukuzhi , C. Sun. "Models for the strain-rate-dependent behavior of polymer composites." Composites science and technology 61 (2001) 1-12.
[4] J. López-Puente , S. Li. "Analysis of strain rate sensitivity of carbon/epoxy woven composites." International Journal of Impact Engineering 48 (2012) 54-64.
[5] S. Marguet, P. Rozycki , L. Gornet. "A rate dependent constitutive model for carbon-fiber reinforced plastic woven fabrics." Mechanics of Advanced Materials and Structures 14 (2007) 619-631.
[6] C. Hochard, P.-A. Aubourg , J.-P. Charles. "Modelling of the mechanical behaviour of woven-fabric CFRP laminates up to failure." Composites science and technology 61 (2001) 221-230.
[7] Z. ming Huang. "The mechanical properties of composites reinforced with woven and braided fabrics." Composites science and technology 60 (2000) 479-498.
[8] X. Bai, M. A. Bessa, A. R. Melro, P. P. Camanho, L. Guo , W. K. Liu. "High-fidelity micro-scale modeling of the thermo-visco-plastic behavior of carbon fiber polymer matrix composites." Composite Structures 134 (2015) 132-141.
[9] R. K. Goldberg , D. C. Stouffer. "Strain rate dependent analysis of a polymer matrix composite utilizing a micromechanics approach." Journal of Composite Materials 36 (2002) 773-793.
[10] S.-Y. Hsu, T. Vogler , S. Kyriakides. "Inelastic behavior of an AS4/PEEK composite under combined transverse compressionand shear. Part II: modeling." International Journal of Plasticity 15 (1999) 807-836.
[11] E. Shafiei , M. S. Kiasat. "A new viscoplastic model and experimental characterization for thermosetting resins." Polymer Testing 84 (2020) 106389.
[12] J. Tang, G. Zhou, X. Wang, C. Li , V. V. Silberschmidt. "Failure analysis of plain woven glass/epoxy laminates: Comparison of off-axis and biaxial tension loadings." Polymer Testing 60 (2017) 307-320.
[13] G. Zhou, X. Wang, C. Li , J. Deng. "Experimental investigation on mechanical properties of unidirectional and woven fabric glass/epoxy composites under off-axis tensile loading." Polymer Testing 58 (2017) 142-152.
[14] L. Xing , K. L. Reifsnider. "Progressive failure modeling for dynamic loading of woven composites." Applied composite materials 15 (2008) 1-11.
[15] J. Lu, P. Zhu, Q. Ji , Z. Cheng. "Experimental study of in-plane mechanical properties of carbon fibre woven composite at different strain rates." Polymers and Polymer Composites 25 (2017) 289-298.
[16] T. Matsuda, Y. Nimiya, N. Ohno , M. Tokuda. "Elastic–viscoplastic behavior of plain-woven GFRP laminates: homogenization using a reduced domain of analysis." Composite Structures 79 (2007) 493-500.
[17] D. Blackketter, D. Walrath , A. Hansen. "Modeling damage in a plain weave fabric-reinforced composite material." Journal of Composites, Technology and Research 15 (1993) 136-142.
[18] C. Medina, C. Canales, C. Arango , P. Flores. "The influence of carbon fabric weave on the in-plane shear mechanical performance of epoxy fiber-reinforced laminates." Journal of Composite Materials 48 (2014) 2871-2878.

[19] A. Adumitroaie , E. J. Barbero. "Stiffness and strength prediction for plain weave textile reinforced composites." Mechanics of Advanced Materials and Structures 19 (2012) 169-183.
[20] A. Adumitroaie and E. J. Barbero. Beyond plain weave fabrics - I. geometrical model. Composite Structures, 93:1424–1432, 2011.
[21] A. Adumitroaie and E. J. Barbero. Beyond plain weave fabrics - II. mechanical properties. Composite Structures, 93:1449–1462, 2011.

[22] V. Ganesh , N. Naik. "Failure behavior of plain weave fabric laminates under on-axis uniaxial tensile loading: I—laminate geometry." Journal of Composite Materials 30 (1996) 1748-1778.
[23] D. Scida, Z. Aboura, M. Benzeggagh , E. Bocherens. "Prediction of the elastic behaviour of hybrid and non-hybrid woven composites." Composites science and technology 57 (1998) 1727-1740.
[24] Y. Kwon , W. Cho. "Multilevel, micromechanical model for thermal analysis of woven-fabric composite materials." Journal of Thermal Stresses 27 (2004) 59-73.
[25] E. J. Barbero, T. M. Damiani , J. Trovillion. "Micromechanics of fabric reinforced composites with periodic microstructure." International Journal of Solids and Structures 42 (2005) 2489-2504.
[26] E. Barbero, J. Trovillion, J. Mayugo , K. Sikkil. "Finite element modeling of plain weave fabrics from photomicrograph measurements." Composite Structures 73 (2006) 41-52.
[27] E. Shafiei, M. S. Kiasat , E. J. Barbero. "Rate-dependent viscoplastic modeling and experimental validation of woven glass/epoxy composite materials." Composites Part B: Engineering(2021) 108827.
[28] S. Waddar, J. Pitchaimani, M. Doddamani , E. Barbero. "Buckling and vibration behaviour of syntactic foam core sandwich beam with natural fiber composite facings under axial compressive loads." Composites Part B: Engineering 175 (2019) 107133.
[29] E. J. Barbero. Introduction to composite materials design, CRC press.(2017).
[30] S. Z. Sheng , S. Van Hoa. "Three dimensional micro-mechanical modeling of woven fabric composites." Journal of Composite Materials 35 (2001) 1701-1729.
[31] N. K. Naik, P. Yernamma, N. M. Thoram, R. Gadipatri , V. R. Kavala. "High strain rate tensile behavior of woven fabric E-glass/epoxy composite." Polymer Testing 29 (2010) 14-22.
[32-] G. Belingardi, H. Mehdipour, E. Mangino , B. Martorana. "Progressive damage analysis of a rate-dependent hybrid composite beam." Composite Structures 154 (2016) 433-442.
[31] R. O'higgins, C. McCarthy , M. McCarthy. "Identification of damage and plasticity parameters for continuum damage mechanics modelling of carbon and glass fibre-reinforced composite materials." Strain 47 (2011) 105-115.